Supporting Information

Flexible Metal Electrodes by Femtosecond Laser Activated Deposition for Human-Machine Interface

Yaqiang Ji,[a, b] *Yuxuan Liao,*[b, c] *Haihui Li,*[b] *Yuhang Cai,*[b] *Dongliang Fan,*[b, c] *Qian Liu,*[b] *Shubin Huang,*[b] *Renjie Zhu,*[b, c] *Shuai Wang,*[b] *Hongqiang Wang,**[, b, ,c d] *Liang Guo**[, b]

[a] School of Mechanical Engineering, Harbin Institute of Technology, Harbin 150080, China

[b] Department of Mechanical and Energy Engineering, Southern University of Science and Technology, Shenzhen 518055, China

[c] Shenzhen Key Laboratory of Biomimetic Robotics and Intelligent Systems, Department of Mechanical and Energy Engineering, Southern University of Science and Technology, Shenzhen 518055, China

[d] Guangdong Provincial Key Laboratory of Human-Augmentation and Rehabilitation Robotics in Universities, Southern University of Science and Technology, Shenzhen 518055, China

* Corresponding author:
Hongqiang Wang, E-mail address: wanghq6@sustech.edu.cn;
Liang Guo, E-mail address: guol3@sustech.edu.cn.

Supplementary Note 1

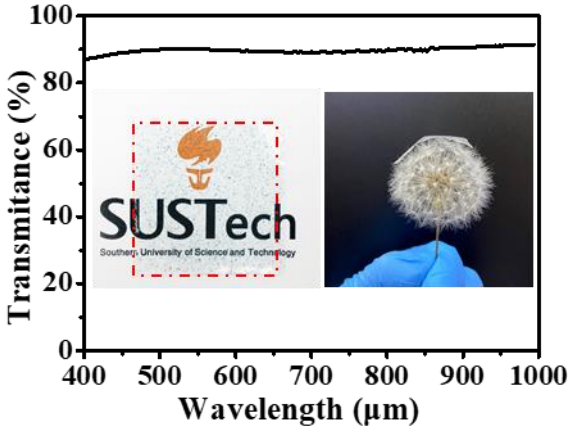

Figure S1. UV-VIS spectrum of PDMS/$CuAc_2$ film with 1 wt % $CuAc_2$. The insets illustrate that the PDMS/$CuAc_2$ film is almost transparent and can stand on a dandelion.

Supplementary Note 2

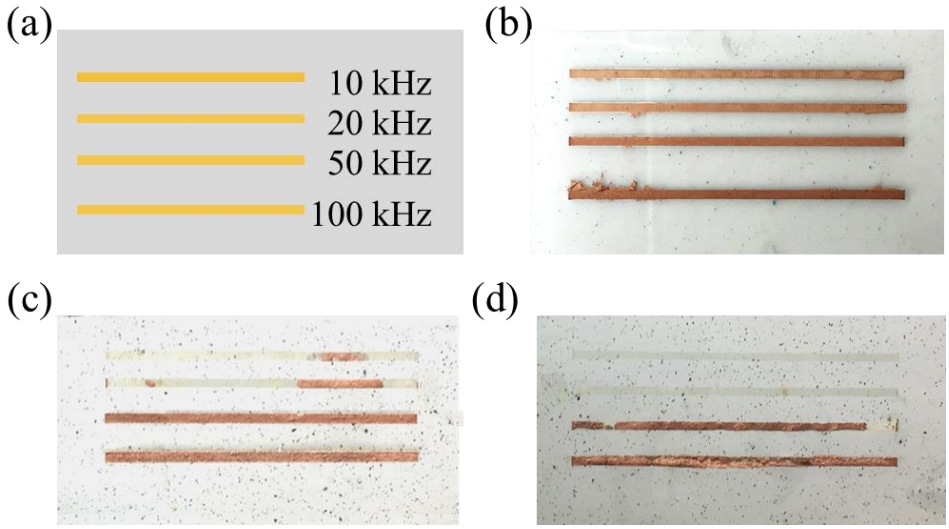

Figure S2. Optical images of the obtained Cu coatings after 60 min ELD at different repetition rates of the femtosecond laser for a specific scanning speed and the same fluence (22 mJ cm^{-2}). (a) Schematic diagram of the sequence for different repetition rates with a specific scanning speed. (b) The Cu coatings for different repetition rates with 5 mm s^{-1} scanning speed. (c) The

Cu coatings for different repetition rates with 10 mm s^{-1} scanning speed. (d) The Cu coatings for different repetition rates with 15 mm s^{-1} scanning speed.

Supplementary Note 3

Laser irradiation usually induces material ablation, causing the splashing of atoms, clusters, particulates, and so on.[1] Although some of them can dissipate into the free space after being ejected from the surface, some may deposit back onto the surface.

Since most of the splashing catalyst particles are absorbed by a dust cleaner (Figures S3a, b), Cu coating is seldom deposited on the unirradiated regions after ELD (Figures S4a, b). However, many particles are distributed in the unirradiated regions without a dust cleaner (Figures S3c, d), which act as seeds for further growth of the Cu coating (Figures S4c, d). Moreover, the sheet resistance of Cu film is 21 mΩ sq^{-1}, measured by a four-point probe system.

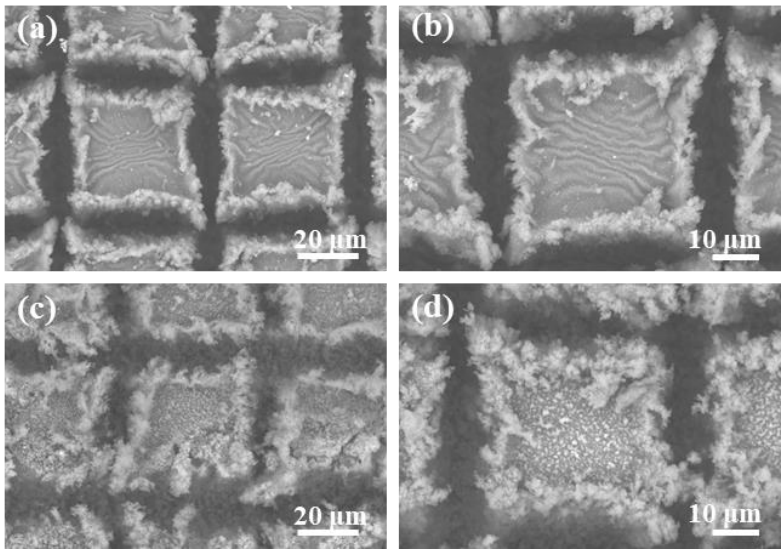

Figure S3. SEM images of the sample after femtosecond laser activation. (a, b) Laser processing with a dust cleaner. (c, d) Laser processing without a dust cleaner.

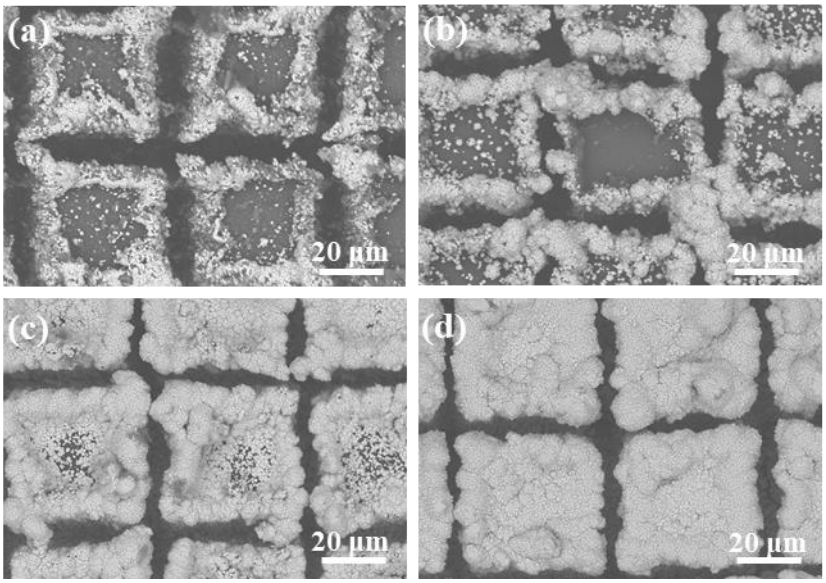

Figure S4. SEM images of the obtained Cu coatings at different deposition times. (a, b) Laser processing with a dust cleaner followed by 40 min and 60 min ELD. (c, d) Laser processing without a dust cleaner followed by 40 min and 60 min ELD.

Supplementary Note 4

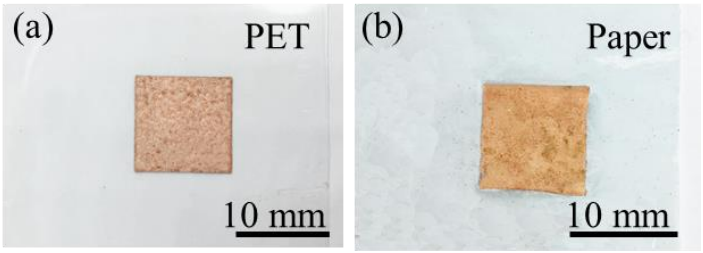

Figure S5. Photographs of the obtained Cu coatings on (a) PET and (b) paper.

Supplementary Note 5

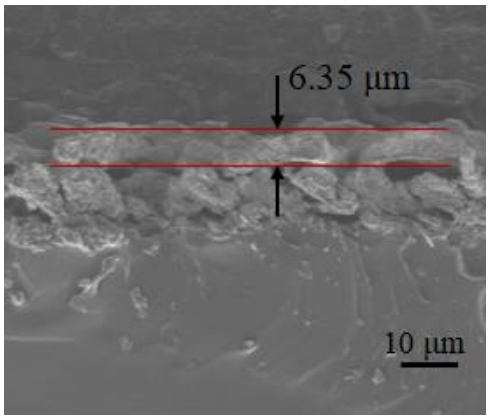

Figure S6. Cross-sectional SEM image of Cu coating on PDMS after 60 min ELD.

Supplementary Note 6

The EDX result (Figure S7) shows that the oxygen EDX peak of the 18-day Cu sample has a higher intensity than that of the fresh sample, suggesting the occurrence of oxidation.[2] Furthermore, CuO is not detected by XPS from Figure S8 indicated by the lack of the satellite peaks belonging to Cu^{2+} compounds. It is known that most XPS instruments cannot resolve the typical peaks of Cu^0 and Cu^+.[3] Fortunately, Cu and Cu_2O could be distinguished from Cu LMM Auger spectra in Figure S9. Compared with the Auger spectrum of Cu^0 (918.6 eV), the peak for the 18-day sample is shifted to the left, indicating the formation of Cu_2O on the surface.[4]

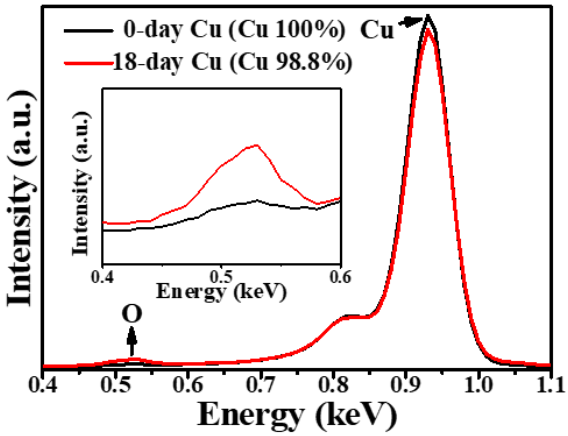

Figure S7. EDX spectra of the Cu coating measured for different exposure times in the air. The inset is a local magnification of the oxygen EDX peak.

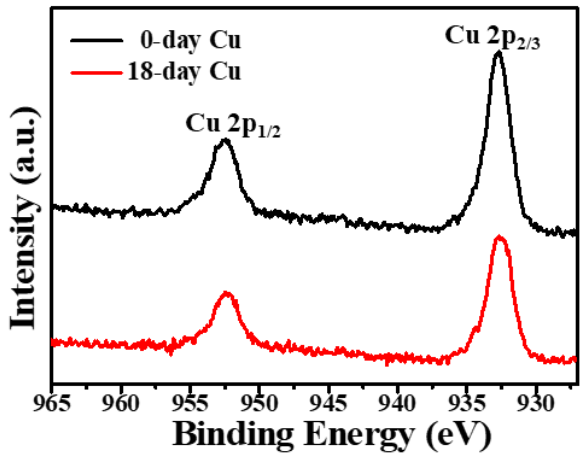

Figure S8. XPS spectra of the Cu coating measured for different exposure times in the air.

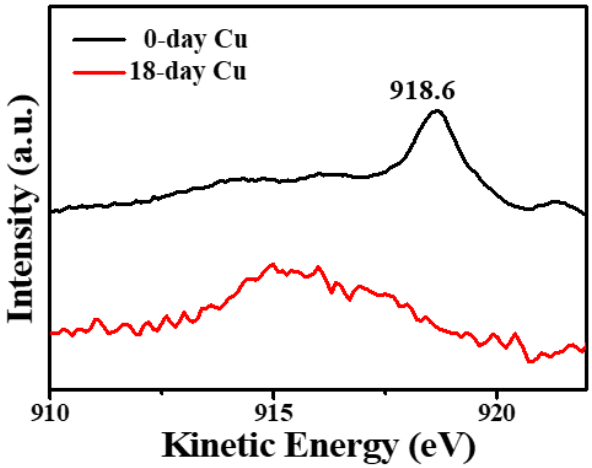

Figure S9. Cu LMM Auger spectra of the Cu coating measured for different exposure times in the air.

Supplementary Note 7

The scotch tape test was used to evaluate the adhesion between the as-prepared Cu coating and the PDMS substrate. The PDMS/Cu film was bent for 10000 cycles at r=3 mm, and then was divided into 100 squares (1 mm × 1 mm each). The film was attached firmly with a piece of 3M tape, which was subsequently peeled off in a direction perpendicular to the surface. None of the cross-hatched squares was stripped, as shown in Figure S10a, suggesting the best level (ASTM D3359). Moreover, only a trace of powders remains on the 3M tape (Figure S10b), which may be

produced by the dividing process. A confocal laser scanning microscope measured the cutting depths, and the depths for both directions are about 20 μm (Figures S10c, d).

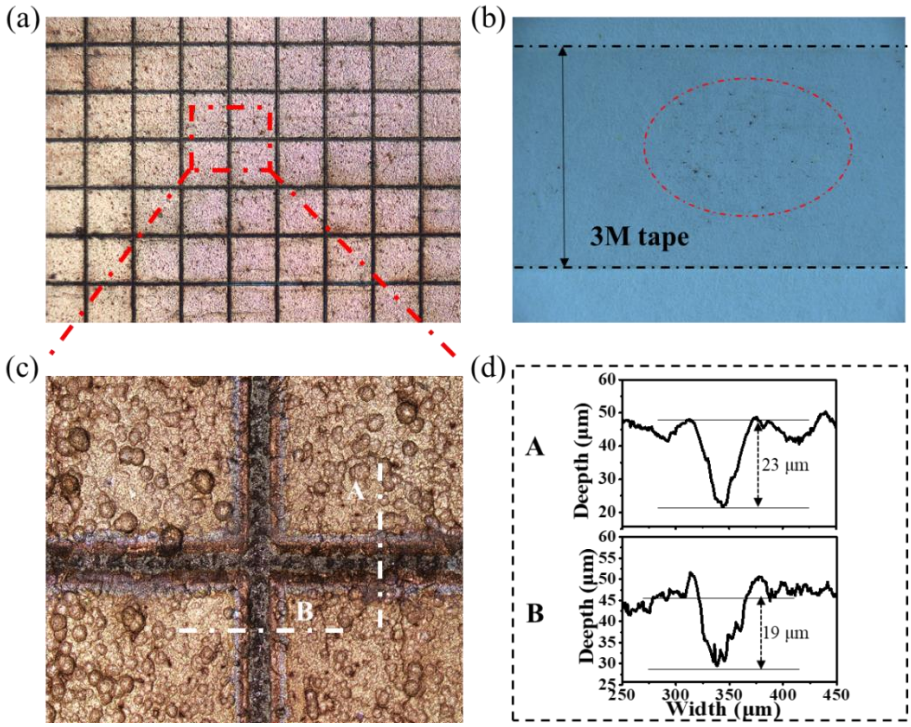

Figure S10. The results of the scotch tape test. (a) Optical image of the sample after 10000 bending cycles. The size of each cell is 1 mm × 1 mm. (b) Optical image of the 3M tape after the scotch tape test. (c) is a local magnification of (a). (d) The cutting depths in both directions in (c) measured by a confocal laser scanning microscope.

Supplementary Note 8

The formation of SiC through thermal decomposition of siloxanes has been studied by previous studies.[5, 6] In brief, siloxane preceramic polymer can convert to SiC when the temperature is above 1400 °C under an inert ambiance, which is attributed to carbothermal reactions and carbon originates from the organic groups. Thermal decomposition exhibits the two-step pyrolysis that consists of the 'regime I' ranging from 500 to 1,400 °C and the subsequent 'regime II' above 1,400 °C.

$$4CH_3SiO_{1.5}\,(s) \rightarrow (CH_3)_4Si\,(s) + 3SiO_2\,(s) \qquad \text{regime I}$$

$$SiO_2\,(s) + 3C\,(s) \rightarrow SiC\,(s) + 2CO\,(g) \qquad \text{regime II}$$

To investigate the temperature change induced by femtosecond laser activation, we devise a temperature detection experiment as shown in Figure S11a. While the laser beam is irradiating on the PDMS surface, a thermal camera monitors the temperature change. At the stationary laser focus, the maximum temperature reaches 350 °C (Figure S11b), which reveals a huge discrepancy with 1,400 °C. During femtosecond laser activation, the temperature should be lower than 350 °C since the sample is moving.

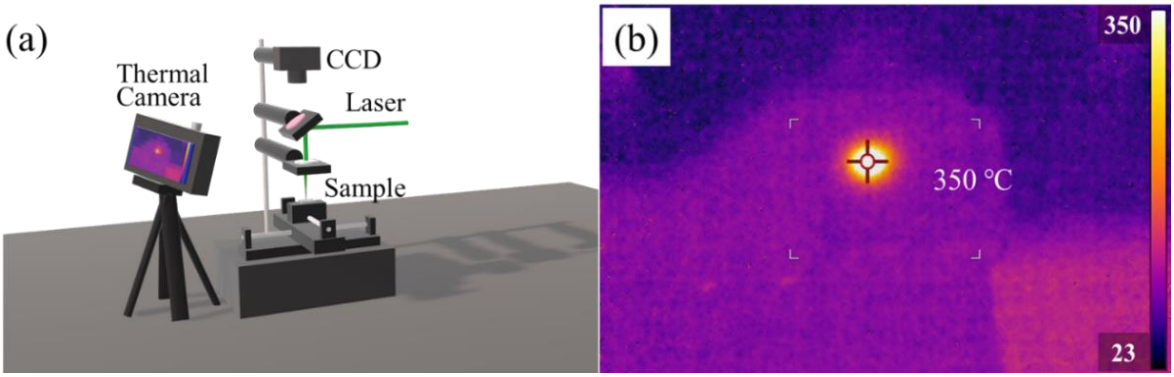

Figure S11. (a) Experimental setup for temperature monitoring by the thermal camera. (b) The image from the thermal camera.

To explain PDMS decomposition at low temperature, a kinetic effect may be involved.[7, 8] The decomposition products of PDMS could be different by changing the heating rates as shown in Figure S12. In the case of slow heating lower than 50 °C min^{-1}, the pyrolysis near 500 °C yields the generation of cyclic oligomers that are thermally stable, which can be explained by Si-O bond scission leading to tight crosslinking of the polymer. Subsequently, the cyclic oligomers could be further decomposed to SiC at a temperature above 1400 °C following the two-step pyrolysis. On the contrary, the higher heating rate of 100 °C min^{-1} induces the domination of Si-C bond scission over the Si-O bond scission, and then SiO_2 is reduced to SiC by carbon. Therefore, rapid heating could generate SiC at 600-700 °C. When it comes to femtosecond laser processing, the heating rate far exceeds the heating ratio of 100 °C min^{-1}. As a result, we anticipate that the femtosecond laser could enable a low-temperature direct SiC derivation.

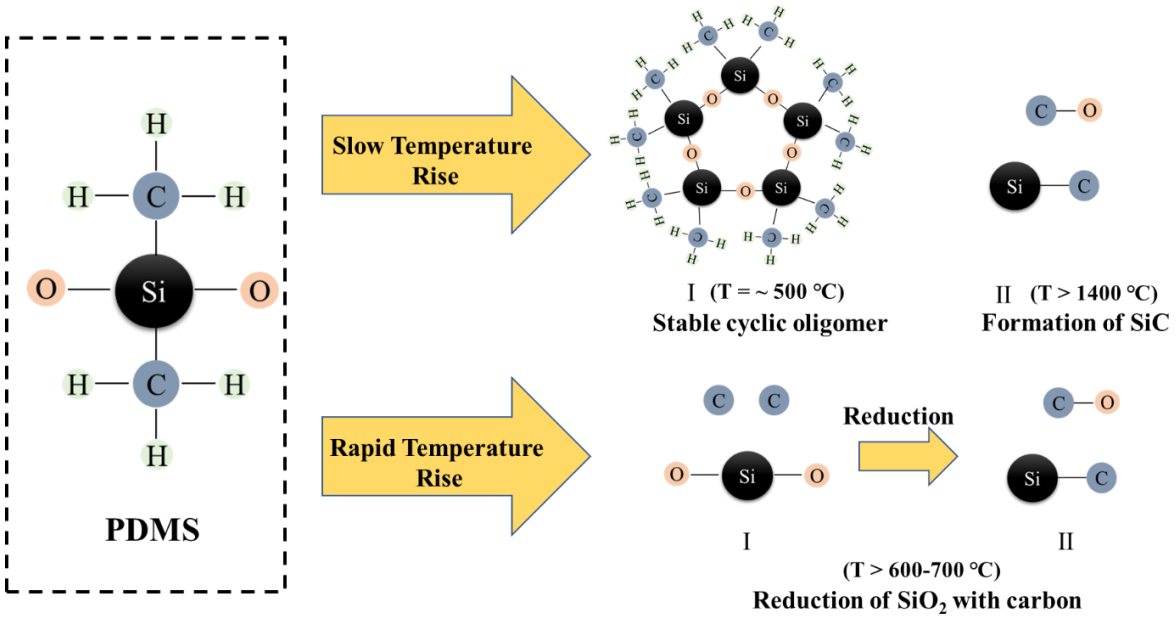

Figure S12. Effect of temperature rise rate on the decomposition of PDMS.

Supplementary Note 9

The thermogravimetry analysis (Figure S13) was carried out to investigate the thermal stability of $CuAc_2$. $CuAc_2$ begins to break down over 250 ℃. It has been reported in many works that organic copper compounds could be decomposed into Cu^0 when the temperature is higher than its decomposition temperature.[9, 10]

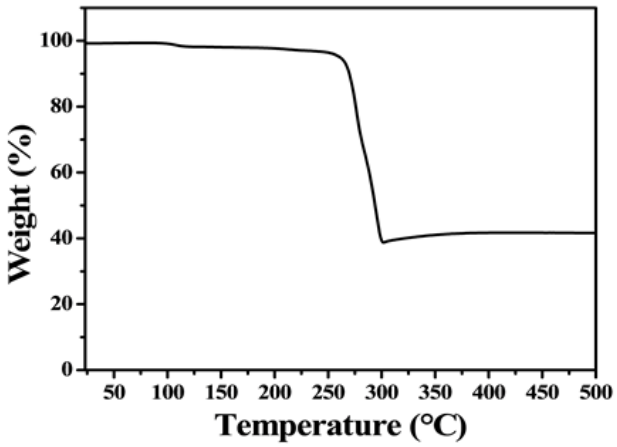

Figure S13. TG curve of $CuAc_2$ upon heating from 30 °C to 500 °C at 20 °C min^{-1} under an air atmosphere.

Supplementary Note 10

The root mean square (RMS) can be expressed as:

$$\mathrm{RMS} = \sqrt{\frac{1}{N}\sum_{i=1}^{N} x_i^2} \qquad (1)$$

where x_i is i th sample in N segments, representing the magnitude of the sEMG signals. A 200 ms sliding window with a 50 ms overlap is used to determine the RMS feature.

Within each epoch, the signal is defined as the maximum of the RMS during the maximum voluntary contraction (MVC Regime), while noise is defined as the average RMS within 3 s under relaxation (Baseline Regime). The SNR is then calculated as the ratio of these two values, as shown in the following equation.

$$\mathrm{SNR(dB)}=20\times\log_{10}\left(\frac{\max(\mathrm{RMS_{MVC}})}{\mathrm{mean}(\mathrm{RMS_{Baseline}})}\right) \quad (2)$$

We use the RMS as the feature for gesture recognition and take these gestures from hand motion as the target of gesture recognition. As shown in Figure S14, we could control a virtual hand to follow the gestures.

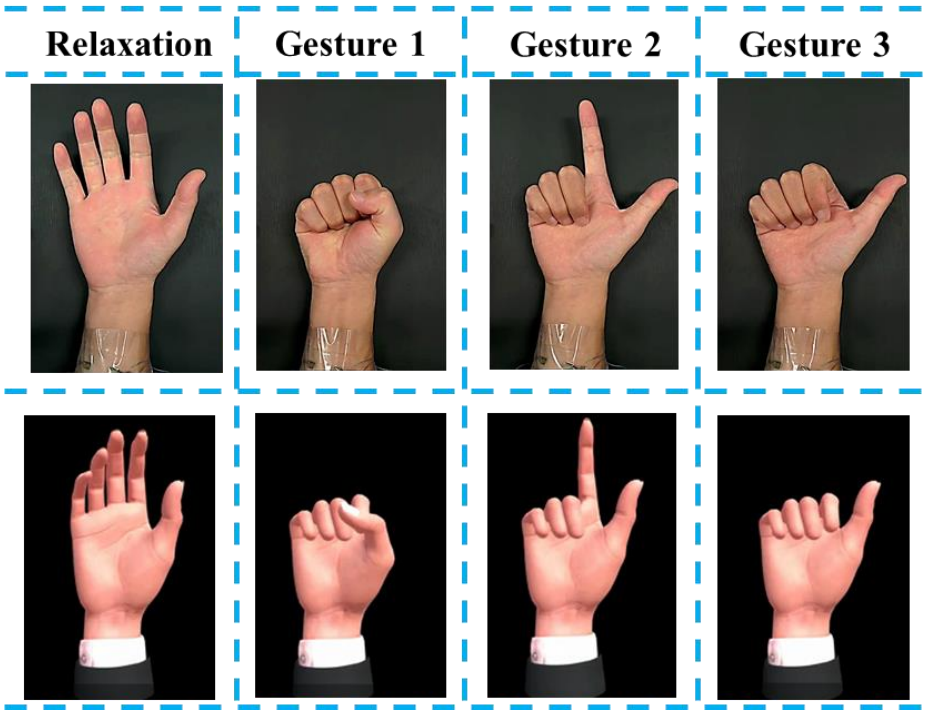

Figure S14. Images showing human hand gestures and the corresponding gestures of a virtual hand.

Supplementary Note 11

According to the characteristics of sEMG signals, we used the random forest machine learning model as the classifier to recognize the gestures. The machine learning model was constructed by extracting time-domain features and adjusting the weight of each feature to realize recognition. As shown in Figure S15, gesture recognition could be divided into offline training of the model and online real-time control. The trained model was used to recognize the real-time input signal of the online real-time control. Figure S16 shows the hardware system, which contains an Arduino Uno

Rev3 board for sEMG signal acquisition, a Raspberry Pi 4B board for data processing, and a robot hand. Original sEMG signals were input to the Raspberry Pi 4B board, and then the results of recognition were sent to the robot hand.

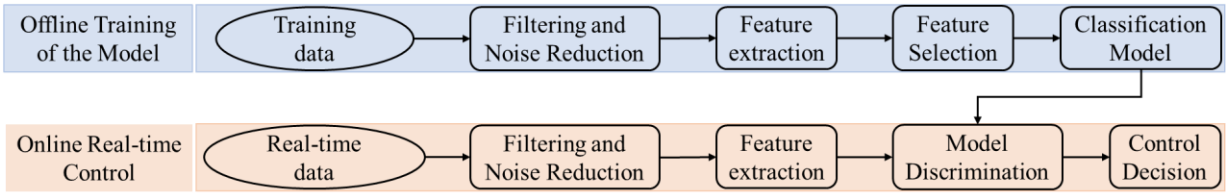

Figure S15. The flow chart of gesture recognition for a robot hand.

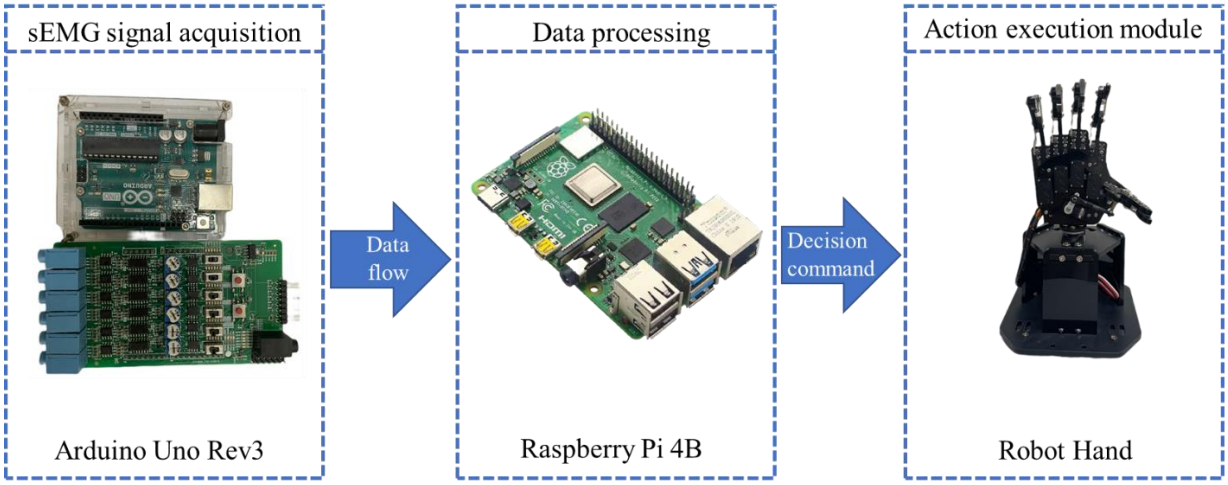

Figure S16. The hardware system of gesture recognition for a robot hand.

Model Training

We used the random forest machine learning model as the classification model because of its good accuracy and efficiency. This classifier uses multiple trees to train and predict samples. The following features are extracted from the time domain.[11] RMS reflects the energy level of the sEMG signal in muscle activity. Mean absolute value (MAV) displays the sEMG signal deviation from the horizontal axis. Waveform Length (WL) is the cumulative length of the waveform over the segment. Zero crossing (ZC) represents the number of intersection points between the sEMG signal and the horizontal axis. Slope sign change (SSC) indicates the number of changes in the

sEMG signal slope sign. These features were sent to the model for training. In this work, the accuracy of the model for static gesture recognition is 95%.

$$\mathrm{MAV} = \frac{1}{N}\sum_{i=1}^{N}\left|x_i\right| \tag{3}$$

$$\mathrm{WL} = \sum_{i=1}^{N}\left|x_{i+1} - x_i\right| \tag{4}$$

$$\mathrm{ZC} = \frac{1}{2(N\text{-}1)}\sum_{i=1}^{N\text{-}1}\left|\mathrm{sgn}\left[x_i\right] - \mathrm{sgn}\left[x_{i+1}\right]\right| \tag{5}$$

$$\mathrm{SSC} = \frac{1}{2(N\text{-}2)}\sum_{i=2}^{N\text{-}1}\left|\mathrm{sgn}\left[x_i\text{-}x_{i\text{-}1}\right] - \mathrm{sgn}\left[x_{i+1}\text{-}x_i\right]\right| \tag{6}$$

where x_i is the i th sample in N segments, representing the magnitude of the sEMG signal.

Real-Time Gesture Recognition

To improve the speed of real-time gesture recognition, a sliding window of 500 ms was adopted and the window shift was set as 50 ms, so the random forest classifier can output 10 times of recognition results per second. The robot hand is not required to accept instructions in the process of executing the action. After 20 tests, the accuracy of real-time identification is 80%.

References

(1) Fan, P.; Bai, B.; Zhong, M.; Zhang, H.; Long, J.; Han, J.; Wang, W.; Jin, G., General strategy toward dual-scale-controlled metallic micro-nano hybrid structures with ultralow reflectance. *ACS Nano* **2017,** *11*, 7401-7408.

(2) Zhou, F.; Li, Z.; Shenoy, G. J.; Li, L.; Liu, H., Enhanced room-temperature corrosion of copper in the presence of graphene. *ACS Nano* **2013,** *7*, 6939-6947.

(3) Dubé, C. E.; Workie, B.; Kounaves, S. P.; Robbat Jr, A.; Aksub, M. L.; Davies, G., Electrodeposition of metal alloy and mixed oxide films using a single‐precursor tetranuclear copper-nickel complex. *J. Electrochem. Soc.* **1995,** *142*, 3357.

(4) Zuo, Z.-J.; Li, J.; Han, P.-D.; Huang, W., XPS and DFT studies on the autoxidation process of Cu sheet at room temperature. *J. Phys. Chem. C* **2014,** *118*, 20332-20345.

(5) Burns, G. T.; Taylor, R. B.; Xu, Y.; Zangvil, A.; Zank, G. A. High-temperature chemistry of the conversion of siloxanes to silicon carbide. *Chem. Mater.* **1992,** *4*, 1313-1323.

(6) Venkatachalam, S.; Lenfant, S.; Depriester, M.; Sahraoui, A. H.; Hourlier, D. Heat treatment of commercial polydimethylsiloxane PDMS precursors: Part II. Thermal properties of carbon-based ceramic nanocomposites. *Ceram. Int.* **2019,** *45*, 21505-21511.

(7) Camino, G.; Lomakin, S.; Lazzari, M. Polydimethylsiloxane thermal degradation Part 1. Kinetic aspects. *Polymer* **2001**, *42*, 2395-2402.

(8) Camino, G.; Lomakin, S.; Lageard, M. Thermal polydimethylsiloxane degradation. Part 2. The degradation mechanisms. *Polymer* **2002**, *43*, 2011-2015.

(9) Obaid, A.; Alyoubi, A.; Samarkandy, A.; Al-Thabaiti, S.; Al-Juaid, S.; El-Bellihi, A.; Deifallah, E.-H. Kinetics of thermal decomposition of copper (II) acetate monohydrate. *J. Therm. Anal. Calorim.* **2000**, *61*, 985-994.

(10) Lin, Z.; Han, D.; Li, S. Study on thermal decomposition of copper (II) acetate monohydrate in air. *J. Therm. Anal. Calorim.* **2012**, *107*, 471-475.

(11) Junior, J. J. A. M.; Freitas, M. L.; Siqueira, H. V.; Lazzaretti, A. E.; Pichorim, S. F.; Stevan Jr, S. L. Feature selection and dimensionality reduction: An extensive comparison in hand gesture classification by sEMG in eight channels armband approach. *Biomed. Signal Process. Control* **2020**, *59*, 101920.